# Structure-based Design of Dual Bactericidal and Bacteria Releasing Nanosurfaces

Daniel Salatto<sup>1</sup>, Zhixing Huang<sup>1</sup>, Peter Todd Benziger<sup>2,3</sup>, Jan-Michael Y. Carrillo<sup>4</sup>, Yashasvi Bajaj<sup>1</sup>, Aiden Gauer<sup>1</sup>, Leonidas Tsapatsaris<sup>1</sup>, Bobby G. Sumpter<sup>4</sup>, Ruipeng Li<sup>5</sup>, Mikihito Takenaka<sup>6</sup>, Wei Yin<sup>7</sup>, David G. Thanassi<sup>2,3</sup>, Maya Endoh<sup>1\*</sup>, Tadanori Koga<sup>1,8\*</sup>

<sup>1</sup>Department of Materials Science and Chemical Engineering, Stony Brook University, Stony Brook, New York 11794-2275

<sup>2</sup>Department of Microbiology and Immunology, Stony Brook University, Stony Brook, New York 11794-5222

<sup>3</sup>Center for Infectious Diseases, Stony Brook University, Stony Brook, New York, 11794-5120

<sup>4</sup>Center for Nanophase Materials Sciences, Oak Ridge National Laboratory, Oak Ridge, Tennessee, 37831

<sup>5</sup>National Synchrotron Light Source II, Brookhaven National Laboratory, Upton, New York, 11973

<sup>6</sup>Institute for Chemical Research, Kyoto University, Uji, Kyoto 611-0011, JAPAN

<sup>7</sup>Department of Biomedical engineering, Stony Brook University, Stony Brook, New York, 11794-5281

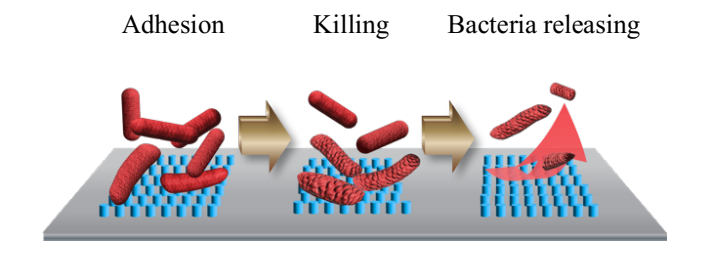
<sup>8</sup>Department of Chemistry, Stony Brook University, Stony Brook, New York, 11794-3400

## **Abstract**

Here, we report synergistic nanostructured surfaces combining bactericidal and bacteria releasing properties. A polystyrene-block-poly(methyl methacrylate) (PS-block-PMMA) diblock copolymer is used to fabricate vertically oriented cylindrical PS structures ("PS nanopillars") on silicon substrates. The results demonstrate that the PS nanopillars (with height of about 10 nm, size of about 50 nm, and spacing of about 70 nm) exhibit highly effective bactericidal and bacteria releasing properties ("dual properties") against Escherichia coli (E. coli) for at least 36 h of immersion in an E. coli solution. Interestingly, the PS nanopillars coated with a thin layer ( $\approx 3$ nm-thick) of titanium oxide (TiO<sub>2</sub>) ("TiO<sub>2</sub> nanopillars") show much improved dual properties against E. coli (a Gram-negative bacterium) compared to the PS nanopillars. Moreover, the dual properties emerge against Listeria monocytogenes (a Gram-positive bacterium). To understand the mechanisms underlying the multifaceted property of the nanopillars, coarse-grained molecular dynamics (MD) simulations of a lipid bilayer (as a simplified model for E. coli) in contact with a substrate containing hexagonally packed hydrophilic nanopillars were performed. The MD results demonstrate that when the bacterium/substrate interaction is strong, the lipid heads adsorb onto the nanopillar surfaces, conforming the shape of a lipid bilayer to the structure/curvature of nanopillars and generating high stress concentrations within the membrane (i.e., the driving force for rupture) at the edge of the nanopillars. Membrane rupture begins with the formation of pores between nanopillars (i.e., bactericidal activity) and ultimately leads to the membrane withdrawal from the nanopillar surface (i.e., bacteria releasing activity). In the case of Gram-positive bacteria, the adhesion area to the pillar surface is limited due to the inherent stiffness of the bacteria, creating higher stress concentrations within a bacterial cell wall. The present study provides insight into the mechanism underlying the "adhesion-mediated" multifaceted property of nanosurfaces, which is crucial for the development of next-generation antibacterial surface coatings for relevant medical applications.

**Keywords:** bactericidal, bacteria releasing, nanopatterned surfaces, block copolymers, titanium oxide

# For Table of Content use only



### 1. Introduction

Biofouling is the undesired accumulation of foreign microorganisms and biological substances on material surfaces. The adhesion of unwanted microorganisms poses numerous associated health risks when designing various medical devices such as catheters, vascular stents, orthopedic implants, artificial heart valves, dental implants, and various extracorporeal tubing. For example, catheter-associated urinary tract infection is the source of nearly 20% of episodes of healthcare associated bacteremia in acute care settings, and nearly 50% of episodes of bacteremia in long-term care facilities<sup>1</sup>. Indwelling catheters provide a surface for the attachment of bacterial adhesins, thereby enhancing microbial colonization and the formation of biofilms<sup>2</sup>. In response to this healthcare challenge, significant efforts have been made to design functional coatings that possess multiple (e.g., antimicrobial and antifouling) properties. However, the development of a multifaceted functional surface coating, which is urgently needed to assist medical professionals and patients, is still challenging due to the different mechanisms underlying the functions.

Surface nanotopography is of great interest for the development of bactericidal surfaces in place of traditional chemical-based approaches that are often toxic to human beings and environments. In addition, the efficiency of chemical-based methods diminishes over time as the concentration of biocidal compounds decreases in the material<sup>3</sup>. The so-called "mechanobactericidal actions" with engineered random or ordered nanostructures inspired by cicada wings, which possess nanopillars with a height of about 150 nm and a spacing between neighboring nanopillars of 150 nm, produce surfaces that facilitate controlled interactions with bacteria. Ivanova and co-workers<sup>3-5</sup> reported experimental evidence that the mechanical and structural response of bacterial cell membranes to the deformational stress (imposed by physical contacts with surface nanostructures) can kill *P. aeruginosa* or other Gram-negative bacteria. A similar concept of engineered nanostructured surfaces to kill bacteria has also been reported<sup>6-9</sup>. However, it should be noted that the mechano-bactericidal actions are not effective against Gram-positive bacteria due to their much stiffer mechanical properties<sup>5, 10</sup>. The stretching degree of Gram-negative bacteria depends on the geometric parameters (especially, height and spacing) of a

nanostructure<sup>11-12</sup>, the interactions between the bacterial cell wall and nanostructured surfaces<sup>5</sup>, the bending/stretching modulus of a bacterial cell membrane<sup>5, 12</sup>, and the elastic deformation of nanopillars during bacterial adhesion<sup>13</sup>. On the other hand, there is also an impaling mechanism where very tall ( $> 1 \mu m$  height), high-aspect ratio (i.e., height/size) nanostructures can pierce a bacterium, resulting in the lysis of bacterial cells<sup>14-15</sup>. Surface hydrophobicity also remains of paramount interest as another demonstrative factor for the mechano-bactericidal effect. However, its role in producing the mechano-bactericidal effect has remained uncleared. For example, Linklater et al.<sup>16</sup> and Valiei et al.<sup>17</sup> reported no significant effects of surface hydrophobicity on the mechano-bactericidal actions, while Boinovich and co-workers<sup>18</sup> demonstrated superhydrophilic substrates as the most desirable surface wettability. Hence, the factors and mechanism that determine the precise antibacterial activity of nanopatterned surfaces are still in debate.

In addition, there is a bottleneck for the use of nanostructured surfaces for bactericidal coatings: the loss of mechano-bactericidal efficacy over time due to accumulations of dead bacteria and debris on the surfaces, possibly hindering their use for repeatable and long-term applications or triggering immune responses and inflammation<sup>19</sup>. Thus, the major challenge of this inevitable accumulation has not been fully addressed. A better understanding of how nanostructured surfaces interact with bacteria is hence crucial for the development of new strategies for the design of multifunctional coatings.

Here, we report a multifaceted nanostructured surface with highly efficient bactericidal and bacteria releasing properties against *E. coli* (a Gram-negative bacterium) and *Listeria monocytogenes* (*L. monocytogenes*, a Gram-positive bacterium). The versatile nanostructured surfaces are fabricated by "block copolymer (BCP) lithography"<sup>20</sup> which offers a simple and effective route to fabricate dense, highly ordered periodic microdomains with easy control of their geometric parameters over arbitrarily large areas<sup>21</sup>. We use polystyrene-*block*-poly(methyl methacrylate) (PS-*block*-PMMA) BCP as a rational model to develop optimal nanostructures with feature sizes of less than 100 nm on solid surfaces. We previously established an approach to induce perpendicular-oriented microdomains in BCP thin films on non-neutral silicon (Si)

substrates<sup>22</sup>. The present study uses PS "nanopillars" (cylindrical microdomains with height of about 10 nm, size of about 50 nm, and interpillar spacing of about 70 nm) oriented in the direction perpendicular to the substrate surface, while the PMMA matrix is removed by a combination of UV exposure and subsequent chemical etching<sup>22-23</sup>. The PS nanopillars exhibit not only highly effective mechano-bactericidal actions<sup>3</sup> but also highly effective bacteria releasing properties against *E. coli* for at least 36 h of immersion in a *E. coli* solution. To further enhance the mechanobactericidal actions of the PS nanopillars, we deposit a very thin layer (about 3 nm thick) of titanium oxide (TiO<sub>2</sub>), which has a much better attraction with *E. coli* than PS such that the degree of stretching of a bacterial membrane is expected to be larger<sup>3</sup>, on the PS nanopillars using atomic layer deposition (ALD). This additional metal oxide coating significantly enhances the bactericidal and bacteria releasing properties against *E. coli*. More importantly, it brings about the dual bactericidal and bacteria releasing properties against *L. monocytogenes* as well.

To understand the mechanisms underlying the dual properties of the very short TiO<sub>2</sub>-coated nanopillars, implicit solvent coarse-grained molecular dynamics (MD) simulations of a lipid bilayer in contact with a substrate containing cylindrical hydrophilic pillars with different lipid-substrate interactions are performed as a simplified model for *E. coli*<sup>24</sup> to complement the experimental results. The MD data indicate that when the bacterium/substrate interaction is strong (greater than 2kT, kT is thermal energy), the lipid heads adsorb onto the nanopillar surfaces, conforming the shape of the lipid bilayer to the structure/curvature of the nanopillars. Membrane rupture occurs when the nanopillars generate sufficient tension within the lipid bilayer clamped at the edges of the nanopillars, leading to the formation of pores between nanopillars (i.e., bactericidal activity) and eventually promoting the cell withdrawal from the nanopillar surface (i.e., bacteria releasing activity). The adhesion-mediated rupture is more pronounced for Gram-positive bacteria since the adhesion area to the nanopillar surface is limited owing to the stiffer mechanical properties, causing higher stress concentrations within the bacterial cell wall at the edge of pillars. Hence, the integrated experimental-computational study provides insight into the roles of microscopic structures in antibacterial and bacteria releasing properties. These findings will be

beneficial for the development of engineered nanocoatings for implemented medical devices, since natural tissue surfaces such as the epithelial layer of blood vessels and heart chambers exhibit morphological features at the nanometer scale<sup>25</sup>.

### 2. Experimental Section

#### 2.1. Materials

Monodisperse cylinder forming PS-block-PMMA ( $M_{\rm w,PS} = 46,000 \text{ g/mol}$ ,  $M_{\rm w,PMMA} = 138,000 \text{ g/mol}$ g/mol,  $M_{\rm w}/M_{\rm n}=1.06$ , Polymer Source Inc.) was used. Additionally, PS with an average molecular weight of  $M_w$ =30,000 g/mol ( $M_w$ / $M_n$ =1.06, Pressure Chemical Co.) was used to prepare a "nonpreferential" surface coating (hereafter assigned as "PS nanocoating") for the development of perpendicularly oriented microdomains in PS-block-PMMA thin films deposited on Si substrates. The details of the sample preparation have been described elsewhere<sup>22</sup>. Si (100) wafers, purchased from University Wafer Inc., were pre-cleaned using a hot piranha solution (i.e., a mixture of H<sub>2</sub>SO<sub>4</sub> and H<sub>2</sub>O<sub>2</sub>, caution: a piranha solution is highly corrosive upon skin or eye contact and is an explosion hazard when mixed with organic chemicals/materials; Extreme care should be taken when handling it) for at least 40 min, subsequently rinsed with deionized water thoroughly. The surface treatments resulted in a hydrophilic native silicon oxide (SiO<sub>x</sub>) layer ( $\approx 2$  nm thick) with a surface roughness of less than 0.5 nm and water contact angle less than 10°. The piranha solutioncleaned Si wafers were further immersed in an aqueous solution of hydrogen fluoride (HF) for 20 s to remove the SiOx layer (hereafter assign as "HF-etched Si"). Notably, due to atmospheric oxygen and moisture, we confirmed that a thin SiO<sub>x</sub> layer of about 1 nm thick was reproduced immediately after HF etching<sup>26</sup>.

To prepare the PS nanocoatings on the HF-etched Si substrates, we incorporated the established solvent-rinsing protocol<sup>22, 26</sup>. The PS nanocoatings are composed of strongly adsorbed polymer chains that lie flat on a solid ("flattened chains")<sup>26-27</sup> with about 2 nm in thickness. In brief, PS thin films of 60 nm in thickness were initially spun coated onto the HF-etched Si with a rotation speed of 3,000 rpm. The spun-coated PS films were then annealed at 150 °C, far above the bulk

glass transition temperature ( $T_g$ ), for 24 h in a vacuum oven at  $10^{-3}$  Torr. The pre-annealed films were solvent-leached with chloroform at room temperature repeatedly until the thicknesses of residual layers remained unchanged. All the nanocoatings were post-annealed at 150 °C for 12 h under vacuum to remove any excess solvent molecules.

The PS nanopillars vertically aligned without the PMMA matrix were then prepared on the HF-etched Si substrate covered with the PS nanocoating (we hereafter assign the substrate as "PS nanocoated Si"). We confirmed that the water contact angle (WCA) of the PS nanocoated Si was  $90 \pm 1^{\circ}$ , which is in good agreement with the bulk PS, indicating that the substrate surface was entirely covered with the PS nanocoating. Since the PS nanocoating is stable even against good solvents<sup>26</sup>, 20 nm-thick PS-block-PMMA films were directly prepared on the PS nanocoated Si via spin coating of the PS-block-PMMA/toluene solutions. Along with the non-preferential PS nanocoatings, the novelty of PS-block-PMMA is the easy control of balanced interfacial interactions at the air-polymer interface using temperature (c.a., 200-250 °C)<sup>28</sup>. We annealed the PS-block-PMMA films on the PS nanocoated Si at 230 °C for 10 minutes and then quenched to room temperature (which is below the glass transition temperatures (100-110 °C) of the bulk PS and PMMA) to freeze the microphase separated structures via the vitrification processes of both blocks. The resultant films were subsequently exposed to UV-light in a nitrogen environment for 5 minutes to crosslink the PS component of the films and further developed by submerging the films in acetic acid for 3 minutes to remove the PMMA component from the films <sup>23</sup>. Finally, the resultant films were placed in deionized (DI) water for 3 minutes to remove any remaining acid from them.

#### 2.2. Ellipsometry Measurements

The thicknesses of the spin-cast films and PS nanocoatings were measured by an ellipsometer (Rudolf Auto EL-II) with a single wavelength of 632.8 nm at an incident angle of 70°. The thicknesses were calculated based on the phase difference and the amplitude ratio upon reflection obtained from ellipsometry measurements, along with a single polymer layer model with fixed

refractive indices of 1.587 for PS<sup>29</sup> and 1.518 for PS-*block*-PMMA, respectively. Note that the refractive index of PS-*block*-PMMA was calculated from the volume fractions of PS and PMMA using the refractive indices of PS and PMMA homopolymers (1.489 for PMMA<sup>29</sup>).

As will be described below, to determine the film thickness of an ALD-grown TiO<sub>2</sub> layer on the PS nanopillars, the spectral reflectance of planar Si wafers coated with varying numbers of TiO<sub>2</sub> ALD cycles was measured by a J.A. Woollam M- 2000FI ellipsometer. The spectral reflectance data were collected and analyzed using the WVASE32 data acquisition and analysis software (J.A. Woollam Co. Inc.). The incidence angle of the light beam was varied from 45° to 75° with an angle step size of 5°, normal to the substrate plane. The reflectance data were collected over the wavelengths ranging from 210 to 1692 nm. The TiO<sub>2</sub> film thickness was determined from an ALD-grown TiO<sub>2</sub> layer grown on a planar Si under the same disposition conditions by fitting the data to a three-layer model (TiO<sub>2</sub>, native SiO<sub>2</sub>, and Si) using the known optical constants of the materials provided by the analysis software.

#### 2.3. Atomic layer deposition (ALD)

TiO<sub>2</sub> is often utilized in biomedical devices and biomaterials due to its positive characteristics including biocompatibility<sup>30,31</sup>. ALD is one of the most promising deposition techniques because of its excellent homogeneity and thickness accuracy<sup>32</sup>. In addition, the surface energy of an ALD-grown TiO<sub>2</sub> layer at room temperature (48.5 mN/m under a similar deposition temperature<sup>30</sup>) is closer to that of *E. coli* (65.1 mJ/m<sup>2</sup> <sup>33</sup>) or *L. monocytogenes* (65.9 mJ/m<sup>2</sup> <sup>34</sup>) than that of PS (40.6 mN/m<sup>26</sup>), allowing us to further discuss the effect of an attractive interaction between the bacterial cell wall and the nanostructured surface on the bactericidal property. As previously optimized<sup>35</sup>, depositing a uniform layer of TiO<sub>2</sub> was performed at 80 °C using a Cambridge Nanotech Savannah S100 ALD system at the CFN. The deposition process of TiO<sub>2</sub> on the PS nanopillars undergoes sequential exposure of titanium (IV) isopropoxide and water vapor. Each precursor was purged with N<sub>2</sub>(g) after each sequential exposure. The density of an ALD grown TiO<sub>2</sub> film at 80°C was reported to be about 3.5 g/cm<sup>3 36</sup>. We confirmed the deposition of TiO<sub>2</sub> on the PS nanopillars using

X-ray Photoelectron Spectroscopy (XPS) (**Figure S1**, **Supporting Information (SI)**). To determine the thickness of an ALD-grown  $TiO_2$  layer on the PS nanopillars, the PS nanopillar samples were exposed alongside planar bare Si substrates, which were further measured with ellipsometry. The average thickness of the ALD-grown  $TiO_2$  on the planar Si substrate after 60 cycles was  $3.0 \pm 0.2$  nm. Hereafter we assign the  $TiO_2$ -coated PS nanopillars as " $TiO_2$  nanopillars". It has been reported that  $TiO_2$  has a unique photocatalytic effect when exposed to UV-light<sup>37</sup>. To differentiate from this photocatalytic effect, samples were kept covered in tin foil and away from UV light before any experiments.

## 2.4. Atomic Force Microscopy (AFM) measurements

The surface morphologies of the PS and TiO<sub>2</sub> nanopillars were studied before and after bacterial adsorption experiments by atomic force microscopy (AFM) (Asylum Research MFP-3D) at the Center for Functional Nanomaterials (CFN) at Brookhaven National Laboratory (BNL). Standard tapping mode measurements were conducted in air using a cantilever, AC160TS-R3, with a spring constant of 26 N/m and a resonant frequency of 300 kHz. The scan rate was 2.44 Hz with the scanning density of 256 lines per frame.

# 2.5. Scanning Electron Microscopy (SEM)

SEM was performed (Hitachi 4800) to identify the microdomain structures of the self-assembled PS-*block*-PMMA films prior to bacteria adhesion experiments. In addition, the *E. coli* morphology was analyzed via a cross-section of the samples after the adhesion experiments.

#### 2.6. Grazing-Incidence Small-Angle X-ray Scattering (GISAXS)

GISAXS measurements were conducted at the 11-BM Complex Materials Scattering (CMS) beamline, NSLS-II, Brookhaven National Laboratory to study the microdomain structures of the PS nanopillars and  $TiO_2$  nanopillars. GISAXS patterns were acquired with a PILATUS 2M detector located at the sample-to-detector distance of 3.03 m. The incident angle ( $\alpha_i$ ) was set to be

 $0.15^{\circ}$  to observe the entire structure of the film. Intensity profiles were measured as a function of the scattering vector,  $q = (4\pi \sin\theta)/\lambda$ , where  $\theta$  is half of the scattering angle and  $\lambda$  is the X-ray wavelength ( $\lambda = 0.092$  nm). The in-plane GISAXS profiles were obtained along the in-plane scattering vector parallel to the film surface ( $q_{xy}$ ) at the scattering vector normal to the film surface  $q_z = 0.30$  nm<sup>-1</sup>. The GISAXS data was analyzed by using Igor Pro 8 using the Irena and Nika macro<sup>38</sup>.

## 2.7. Water contact angle (WCA) experiments

The surface energy of the developed films was measured by using an Ossila contact angle meter. WCA measurements were conducted at room temperature under humidity-controlled conditions by using 20  $\mu$ l of water for each sample. The contact angle plugin in ImageJ was utilized to analyze the water droplet on the sample surface. We also confirmed that the effect of UV exposure (5 mins), which was used to cross-link a PS component, on the WCA was minimal (Figure S2).

#### 2.8. Bacterial Strains, Growth Conditions and Staining Protocols

E. coli K12 (ATCC #25404) or L. monocytogenes was used in experiments to determine the antimicrobial effects of the surface nanotopographies. Both E. coli and L. monocytogenes were grown in standard LB broth at 37 °C with shaking (200 rpm) prior to the start of each experiment. To determine the ratio of live to dead bacteria after incubation, the films were placed in a sterile 12-well plate with the nanostructured surface faced upward. As a control, planar PS and ALD-grown TiO<sub>2</sub> film prepared on Si substrates were used. Both E. coli and L. monocytogenes were diluted to an OD<sub>600</sub> of 0.1 ( $\sim$ 1.0×10<sup>7</sup> colony forming units/mL) and 2-mL of culture were added to each well containing different nanostructures for the indicated time at 37 °C with no shaking. To visualize the total amount of bacteria attached to the nanostructured surfaces or suspended in LB broth, bacteria were stained with the cell-permeable dye, Hoescht 33342, at a final concentration of 0.5  $\mu$ g/mL. In addition, the total amount of dead bacteria or bacteria with

disrupted cell walls was visualized by adding Propidium Iodide (PI) at a final concentration of 0.5  $\mu$ g/mL. The dyes were added together in each well containing both bacteria and polymer 30 minutes prior to sample collection to avoid causing false positives by overstaining bacteria. Prior to microscopy experiments, samples were gently rinsed with 1 mL of DI water to remove the loosely adsorbed bacteria on the nanostructures and then gently dried with a flow of oxygen. An EVOS FL Auto microscope was utilized to further examine the stained bacteria adsorbed on the nanostructured surfaces and bacteria swimming in solution.

## 2.9. Fluorescence Microscopy

An EVOS FL Auto microscope was utilized to analyze the presence of *E. coli* or *L. monocytogenes*. The cell permeable dye Hoechst 33342 was used to visualize both live and dead bacteria and the PI dyes, which is not permeant to live cells, was used to visualize dead bacteria and were selected to analyze the "alive" and "dead" bacteria. The ImageJ software was utilized to analyze and count the number of adsorbed bacteria cells on the sample surface, differentiating the fluorescence by color. A program was made to count the number of adsorbed bacteria. It separated the fluorescent proteins by color and counted the remaining adsorbed cells. In addition, the program was set to only count objects consistent with the characteristic sizes of *E. coli*  $(1-5 \mu m$  in length)<sup>39</sup> or *L. monocytogenes*  $(0.5-2 \mu m$  in length)<sup>40</sup>. The program was also developed to aid with counting the nuclei of the cells, which provided an increase in contrast when determining the number of cells adsorbed onto the nanopillar surfaces. To check the reproductivity of test results, we prepared three samples for each system. We scanned at least 5 different fields for each sample and the average adhesion data over the three samples were determined and analyzed for statistical significance.

#### 2.10.MD simulations

Motivated by previous integrated experimental and computational work on antimicrobial properties of nanostructured surfaces against  $E.\ coli^{24}$ , our simulation model assumes a planar lipid bilayer (i.e., an outer membrane of  $E.\ coli$ ) as an extremely simplified model for  $E.\ coli$  to

predict and analyze the bacterial interaction with the nanopillar surfaces at the molecular level. Note that Gram-positive bacteria do not have an outer membrane and are encapsulated by a peptidoglycan layer instead<sup>41</sup>. Hence, the same MD simulations can't be directly applicable to L. monocytogenes. However, the computational results for E. coli can help us understand the bactericidal and bacteria releasing properties of the TiO<sub>2</sub> nanopillars against L. monocytogenes which will be described below. Implicit solvent coarse-grained MD simulations of a lipid bilayer, which is in contact with a substrate containing cylindrical hydrophilic pillars with different lipidsubstrate interactions, were performed by using the software package LAMMPS<sup>42</sup>. The lipid bilayer is arranged into a plane spanning the transverse plane of the periodic boundaries of the simulation box (Figure S3). This configuration represents infinitely large vesicles. The substrate consists of Lennard-Jones beads arranged in a hexagonal closed-pack lattice where cylindrical pillars are carved. The configuration of the pillars is arranged in a hexagonal lattice with a defined diameter (d), height (h), and distance ( $D_i$ ) between pillars to mimic the experimental conditions. In these simulations, lipids are modeled using a modified version<sup>43</sup> of the force-field developed by Cooke and co-workers<sup>44</sup>, where a lipid molecule is described by three connected beads consisting of a lipid head-bead and two lipid tail beads. The head-head and head-tail bead pair-wise interactions of the lipids are purely repulsive, while the tail-tail interactions are long-ranged and attractive<sup>44</sup>. The solvent is modeled implicitly, and the temperature is controlled via a Langevin thermostat. The bead connectivity is done by defining anharmonic FENE bonds<sup>45</sup>, and the lipid molecules are kept rigid and rod-like by applying a bending angle potential. Table S1 summarizes the force-field potential energy equations and their corresponding parameters used in the simulations. In the table, we refer to the head, tail, substrate, and base beads as "H", "T", "S", and "B", respectively. The simulations are represented in reduced units where  $\sigma$  is the characteristic bead size, kT is thermal energy, the simulation time is  $\tau = \sigma(m/kT)^{1/2}$ , and m is mass. Typically,  $\sigma$  is in the order of 1 nm<sup>46</sup> and  $\tau$  is in the order of 1 ns. The simulation proceeded for  $6 \times 10^4 \tau$ that is beyond the elapsed time wherein the total system energy has reached its equilibrium value (see Figure S4).

It is generally accepted that bacterial adhesion on a solid surface can be qualitatively predicted by the thermodynamic adhesion energy  $(\Delta F)^{47}$ , which can be described as follows:

$$\Delta F = \gamma^{bs} - \gamma^{bl} - \gamma^{sl}, (1)$$

where  $\gamma^{bs}$ ,  $\gamma^{bl}$ ,  $\gamma^{sl}$ , are the interfacial free energies of the bacteria-solid, bacteria-liquid, and solid-liquid interfaces, respectively. Since the contact angles of the PS and TiO<sub>2</sub> nanopillars (i.e.,  $\gamma^{sl}$ ) are nearly the same and  $\gamma^{bl}$  is fixed,  $\gamma^{bs}$  can be used as a thermodynamic criterion for predicting bacterial adhesion, as Zhang and co-workers<sup>33</sup> proposed for predicting bacterial adhesion on hydrophobic surfaces.

The interfacial energy ( $\gamma^{bs}$ ) of the bacterium-solid interface can be calculated from the corresponding surface energies via appropriate combining rules<sup>48</sup>. Using Neumann's equation of state,  $\gamma^{bs}$  is expressed as

$$\gamma^{bs} = \gamma_b + \gamma_s - 2\sqrt{\gamma_b \gamma_s} e^{-\beta(\gamma_b - \gamma_s)^2} , (2)$$

where the value of  $\beta$  is determined experimentally to be  $1.247 \times 10^{-4}$  (mJ/m²)<sup>-2</sup> <sup>49</sup>, and  $\gamma_b$  and  $\gamma_s$  are the surface energies of a bacterium and substrate, respectively. The surface energy values of PS, ALD-grown TiO<sub>2</sub> (at a similar deposition temperature), and *E. coli*. are 40.6 mN/m² <sup>26</sup>, 48.5 mN/m² <sup>30</sup>, and 65.1 mJ/m² <sup>33</sup>, respectively. Substituting these values into eq. (2) gave us  $\gamma^{bs} = 5.0$  mJ/m² for the *E. coli*/TiO<sub>2</sub> nanopillar system, which is approximated to 8 kT <sup>50</sup>. While we can also estimate  $\gamma^{bs} = 10.3$  mJ/m² for the *E. coli*/PS nanopillar system, the PS nanopillars are, to some extent, covered with residual PMMA chains ( $\gamma_s$ =41.0 mN/m²)<sup>51</sup>, as will be discussed below, such that the  $\gamma^{bs}$  value may be underestimated. Nevertheless, a better bactericidal action of the TiO<sub>2</sub> nanopillars compared to the PS nanopillars is expected, as will be shown in Fig. 4a. Therefore, we chose the lipid head-to-substrate interaction energies ( $\varepsilon_{H-S}$ ) of 1 kT, 2 kT, 4 kT, and 8 kT (similar to the TiO<sub>2</sub>/*E. coli* interaction) to provide insight into the role of the lipid-substrate interaction on the bactericidal property of nanopattern surfaces.

#### 3. Results and Discussion

# 3.1. Characterization of the two nanopillars

We begin with the characterization of nanopattern surfaces. **Figure 1** shows the surface morphologies of (a) the PS nanopillars and (b) the TiO<sub>2</sub> nanopillars. We confirmed that the surface morphology remained unchanged before and after ALD deposition except the size of the pillars became slightly larger. A representative cross-sectional AFM image of the TiO<sub>2</sub> nanopillars is shown in **Figure 1c**, where the diameter (*d*), height (*h*), distance ( $D_i$ ), and surface roughness ( $R_s$ ) can be quantified. A representative cross-sectional AFM image of the PS nanopillars is shown in **Figure S5a**. These parameters are summarized in **Table 1**. In parallel, we also performed GISAXS experiments to provide the statically averaged information about *h* and  $D_i$  over a sufficiently large sample area. A representative GISAXS 2D pattern from the TiO<sub>2</sub> nanopillars is shown in **Figure S6**. **Figure 1d** shows the 1D GISAXS profile along the *q* direction parallel to the film surface ( $q_{ij}$ ) for the TiO<sub>2</sub> nanopillars where the <10> peak at  $q_{<10>}$  =0.11 nm<sup>-1</sup> is identified. From the peak

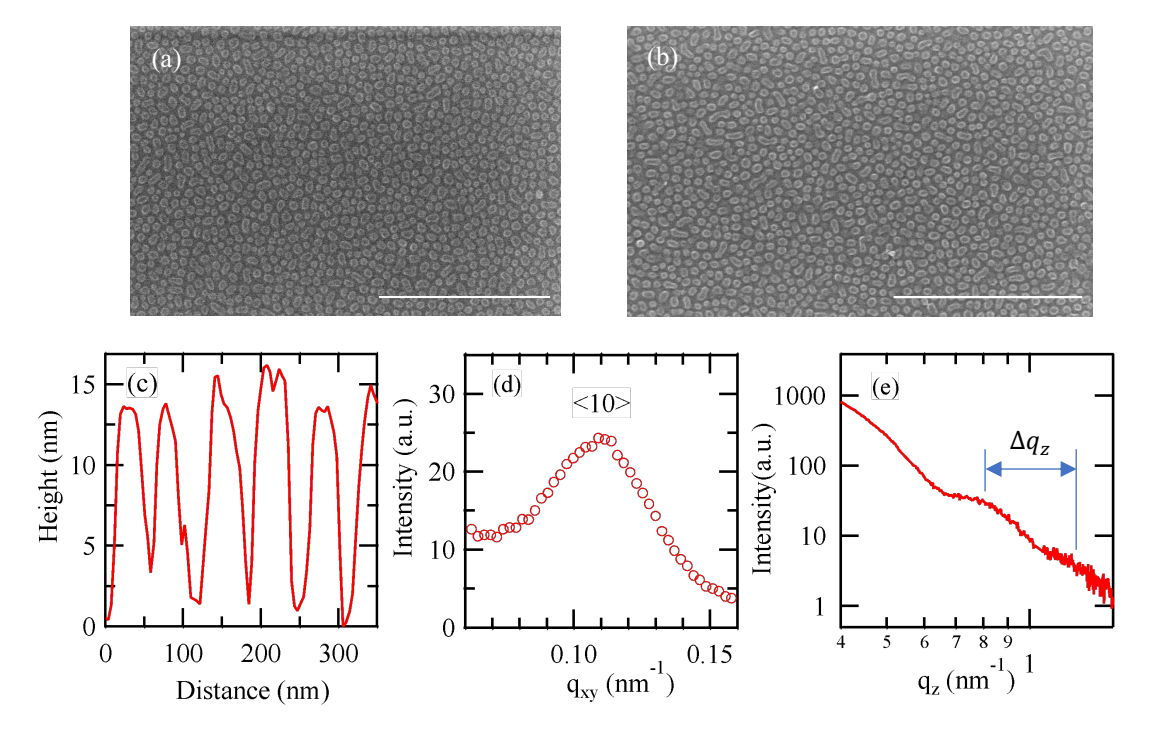


**Figure 1**. Representative SEM images of (a) PS nanopillars and (b)  $\text{TiO}_2$  nanopillars. The scale bar represents 1  $\mu$ m. (c) Cross-sectional image of the AFM height image of the  $\text{TiO}_2$  nanopillars. (d) Representative GISAXS profile along  $q_{xy}$  at  $q_z$ = 0.31 nm<sup>-1</sup> and (e) GISAXS profile along the <10> Bragg rod for the  $\text{TiO}_2$  nanopillars. The distance between the two fringes is related to the average height of  $\text{TiO}_2$  pillars including the native oxide layer and PS nanocoating, as described in the main text.

position, the average nearest-neighbor distance of the pillars,  $D_i = 4\pi/\sqrt{3}q_{<10>} = 66 \pm 1$  nm, was obtained, which is consistent with the AFM result (**Figure 1c**). A representative 1D GISAXS profile as a function of  $q_{ll}$  for the PS nanopillars is shown in **Figure S5b**. The average h values of the respective nanopillars can be calculated from  $2\pi/\Delta q_z$ , where  $\Delta q_z$  is the distance in the scattering vector normal to the film surface  $(q_z)$  between two neighboring fringes seen in the 1D GISAXS profile along the 10 Bragg rod (in the  $q_z$ -direction) (**Figure 1e and Figure S6**). As summarized in **Table 1**, the h values determined from the GISAXS results were in reasonable agreement with the AFM results (**Figure 1c**).

## 3.2. Contact angle results

The apparent WCA ( $\theta_c$ ) (obtained in five measurements) in equilibrium for these nanopatterns are tabulated in **Table 1**. From the table, the PS and TiO<sub>2</sub> nanopillars showed very similar apparent WCA ( $\theta_c = 51\text{-}52\,^{\circ}$ ). As shown in **Figure S7**, the apparent WCA of the PS and TiO<sub>2</sub> nanopillars showed a decrease with time up to  $\sim 5$  h and saturated to the final values tabulated in **Table 1**. Since the WCA on a planar PS surface ( $\theta_F$ ) is 90°, this drastic change in the apparent WCA of the PS nanopillars is indicative of residual PMMA chains even after the PMMA removal using the UV exposure followed by a wet acetic acid treatment, as reported by Delalande and co-workers who demonstrated the presence of residue PMMA chains which partially covered PS nanopillars after an acetic acid treatment using X-ray Photoelectron Spectroscopy (XPS)<sup>52</sup>. Motivated by their results, we performed XPS experiments for the PS nanopillars and confirmed residue PMMA chains on the PS nanopillars (see, Figure S8).

**Table 1**. Characteristics of the nanostructured surfaces used in this study.

Code name	$D_i  (\mathrm{nm})^1$	h (nm) <sup>1</sup>	$d  (\text{nm})^2$	$R_{\rm s}  ({\rm nm})^2$	$\theta_c$ (°) <sup>3</sup>
PS nanopillars	66 <u>±</u> 2	11 <u>±</u> 2	44 <u>±</u> 2	2.8±0.5	51 <u>±</u> 1
TiO <sub>2</sub> nanopillars	66 <u>±</u> 2	14 <u>±</u> 2	46 <u>±</u> 2	5.5±0.5	52±1

1) Determined from GISAXS results

<sup>2)</sup> Determined from AFM results

3) Equilibrium water contact angle under humidity control

On the other hand, the WCA on a planar TiO<sub>2</sub> surface is  $\theta_F = 55^\circ$  such that the apparent WCA for the TiO<sub>2</sub> nanopillars is slightly smaller than  $\theta_F$ . For a hydrophilic rough surface, the effect of surface topography on wetting is discussed in the context of either the super-hydrophilic "hemiwicking" state<sup>53</sup> in which water spontaneously penetrates the cavities and travels beyond the apparent drop, or the Wenzel theory<sup>54</sup>. As shown in **Figure 1** and **Table 1**, our patterned surfaces are rather rough and exhibit distributions in shape and geometric factors. Hence, quantitative discussion about the WCA in conjunction with the theory is challenging, as summarized in the **SI**. It should be noted that the deviations between the measured WCA and the classical models may be also related to atomic scale surface modifications (or defects) of engineered nanopillar surfaces induced during the fabrication process, as recently reported by Xu and co-workers<sup>55</sup>. Here we instead show evidence of the complete wetting on our nanopatterned surfaces using GISAXS.

As mentioned above, the WCA of the PS and TiO<sub>2</sub> nanopillars saturated to the final values after about 5 h. To confirm the penetration of water into the nanostructured surfaces, we performed GISAXS for the PS and TiO<sub>2</sub> nanopillars in contact with a water droplet. A drop of ultrapure water ( $\sim 2~\mu$ l) was gently placed on the samples with a micropipette, and time resolved GISAXS measurements were performed. The scattering intensity from the nanopillars is due to the contrast between the electron density ( $\rho$ ) of the nanopillar ( $\rho_p$ ) and the medium filling the cavities ( $\rho_m$ ). If the liquid medium fills the cavity to a uniform depth, the scattering intensity is well approximated to

$$I \propto (\rho_p - \rho_m)^2$$
. (3)

Hence, when the cavity is filled with water, the scattering intensity is reduced sensitively due to the larger  $\rho$  value of water ( $\rho_w$ =3.34 × 10<sup>23</sup> (e/cm³)) compared to the air. Checco and coworkers<sup>56</sup> formulated the relationship between the volume fraction of a hexagonal cavity, which is filled with water ( $\phi_w$ ), and the ratio between the <10> peak intensity of the wet and dry surface,  $\delta I$ :

$$\phi_w = \frac{\rho_p}{\rho_w} (1 - \delta I). (4)$$

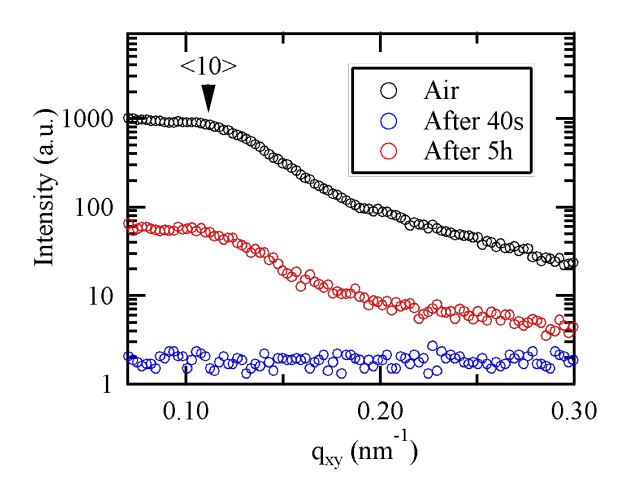


**Figure 2.** GISAXS profiles from the  $TiO_2$  nanopillars as a function of  $q_{xy}$  during the evaporation process of a water droplet on the nanopillars.

 $\rho_p$  of the TiO<sub>2</sub> nanopillars was estimated to be  $\rho_p$ = 4.76 ×10<sup>23</sup> (e/cm<sup>3</sup>), assuming that the TiO<sub>2</sub> nanopillars are composed of the inner PS nanopillars and an outer homogeneous 3 nm thick TiO<sub>2</sub> layer.

At the early stage of an evaporation process under air flow, there were significant contributions from water molecules which give rise to the broad scattering maximum at  $q = 20 \text{ nm}^{-1.57}$  (**Figure S9**), rendering the scattering from the TiO<sub>2</sub> or PS nanopillars invisible (**Figure 2**). However, as evaporation continued, the contributions from water gradually decreased and the <10> peak from the TiO<sub>2</sub> nanopillars appeared after 3h of air flow. The GISAXS profiles from the nanopillars remained unchanged after 5h until at least 24h, similarly to the macroscopic contact angle measurements (**Figure S7**).  $\delta I$  at the <10> peak position (i.e.,  $q_{<10>}=0.11 \text{ nm}^{-1}$ ) was estimated to be 0.064 after drying for 5h. Eq. (4) with this  $\delta I$  value gave us  $\phi_w \approx 1.0$ , indicating that water penetrates the cavities completely. The GISAXS and WCA data are consistent with previous results  $^{56,58}$  on hydrophilic surfaces where air bubbles entrapped within nanopatterned surfaces are gradually replaced with water during water immersion. This replacement may also cause a loss in an antifouling property and promote bacterial colonization  $^{58}$ . However, as will be discussed later, our results demonstrate that the bactericidal and bacteria releasing properties of the TiO<sub>2</sub> and PS

nanopillars remain active over the course of at least 36 h of bacteria exposure. Hence, the emerging functionalities of the nanopillars are not attributed to air bubbles.

It is expected that water also penetrates the cavities of the PS nanopillars (with the residual PMMA chains) completely since the contact angle is nearly the same as that of the TiO<sub>2</sub> nanopillars. However, the residual PMMA chains attached to the PS chains hinders the determination of the exact  $\rho_p$ . In-situ water evaporation GISAXS experiments with the PS nanopillars gave us  $\delta I \approx 0.0085$  after the complete water evaporation. If complete wetting is achieved, this  $\delta I$  value gives us  $\rho_p \approx 3.7 \times 10^{23}$  (e/cm<sup>3</sup>), which is in between the  $\rho$  values of pure PS ( $\rho_{PS}$ =3.37×10<sup>23</sup> (e/cm<sup>3</sup>) and PMMA ( $\rho_{PMMA}$ =3.83×10<sup>23</sup> (e/cm<sup>3</sup>)) and may be qualitatively reasonable.

## 3.2. Antimicrobial properties of the nanopillars

Previous reports showed that the bactericidal action of nanostructured surfaces occur immediately after seeding with bacteria<sup>4</sup> and the bacterial killing efficiency maximizes after a few hours of incubation<sup>59</sup>. In addition, E. coli incubated in LB medium undergoes a loss of viability of  $\sim 99\%$  of the cells after 3 days, regardless of the environmental conditions<sup>60</sup>. As will be discussed later, we therefore set the maximum incubation time to 36 h and confirmed that the natural death ratio of E. coli is much lower than the percentage of dead E. coli in the LB broth taken after submersion of the samples. We hence set the incubation times ranging from 1 h to 36 h of samples being completely submerged in an E. coli solution. Prior to microscopy experiments, all the samples including the counterpart planar PS and TiO2 thin films were gently rinsed with DI water to remove any non-adherent bacteria on the surfaces and then dried with an oxygen flow. The microscopy images in Figure 3 provide insights into the overall performance of the experimental films. From the images, we can see that both nanopillars significantly reduce the total amount of E. coli (both alive and dead ones) bound to the surfaces compared to the counterpart planar substrates. Especially, as shown in Figure 3b, very few bacteria remain bound to the TiO<sub>2</sub> nanopillars. The E. coli adhered on the PS nanopillars are most likely killed (Figure 3a). Moreover, the SEM image in **Figure 3d** shows that *E. coli* spread and adhered to the PS nanopillars after a

couple of hours, while they keep the original rod-like shape. However, as time goes by, the bacteria are eventually punctured on the nanopillars (**Figure 3e**). We will discuss the mechanism later.

**Figure 4a** summarizes the incubation time dependence of *E. coli* adhesion on the two pillars along with the control planar substrates. It should be noted that the numbers include both alive and dead *E. coli*. The control experiments showed that *E. coli* adheres to the planar TiO<sub>2</sub> surface several times more than the planar PS substrate after 4 h incubation time, while the ratio of dead bacteria to the total amount of *E. coli* adhesion are similar each other. This corroborates a better interaction of TiO<sub>2</sub> with *E. coli* compared to PS. Remarkably, the PS nanopillars and TiO<sub>2</sub> nanopillars exhibit extremely low bacterial adhesion compared to the planar PS and TiO<sub>2</sub> surfaces across the entire time domain. It is known that bacteria preferentially adhere to the grooves and spaces in microtextured substrata, which they can colonize the recessed regions only if the grooves/recesses

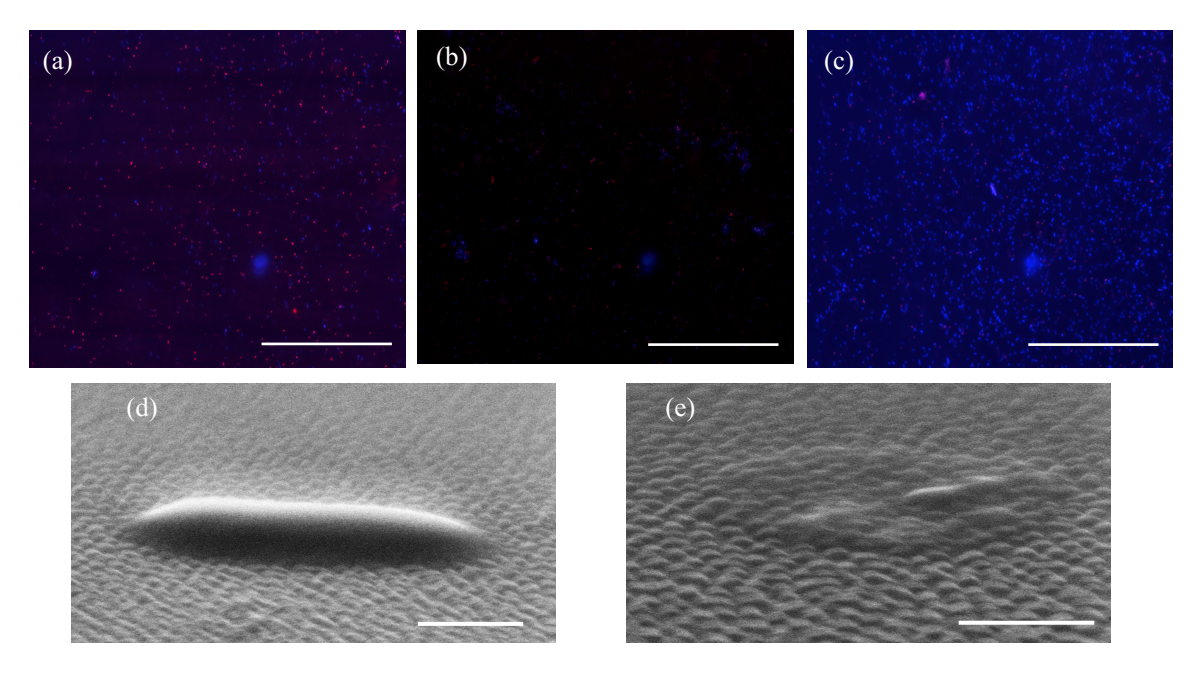


**Figure 3**. Representative fluorescent microscopy images of (a) the PS nanopillars, (b) the  $TiO_2$  nanopillars, and (c) the PS thin film (20 nm thickness) after 12 h of immersion in a *E. coli* solution. The scale bars for (a)-(c) represent 200  $\mu$ m. The Hoechst 33342 stains all bacteria blue, while the PI stains the dead bacteria red. Note that there is an artificial "blue" reflection on the bottom right of the images. SEM images of (d) *E. coli* spreading and adhesion to the PS nanopillars and (e) *E. coli* eventually punctured on the PS nanopillars. Note that we chose the area of focus where the event took place. As shown in Figure 4a, most of the PS and  $TiO_2$  nanopillar surfaces are debris-free. The scale bars for (d) and (e) represent 0.3  $\mu$ m.

are larger than or approximately equal to their own size<sup>3</sup>. Hence, substratum roughness has been deemed one of the most important surface characteristics for control of microbial attachment and the initial stage of biofilm formation<sup>16</sup>. As tabulated in **Table 1**, the dimensions of characteristic the nanostructured surfaces used in this study are much smaller than the length scale of E. coli (a rodlike shape of 1-5  $\mu m$ )<sup>39</sup>, reducing the number of available attachment points with the nanostructured surfaces. Interestingly, the TiO<sub>2</sub> nanopillars reduced the amount of adhered E. coli by 97-98 % compared to the counterpart flat TiO<sub>2</sub> layer after 4 h and 36 h of immersion in a bacterial suspension. In addition, the number of adherent E. coli on the TiO<sub>2</sub> nanopillars became nearly zero and remained unchanged for up to 36 h of immersion, demonstrating a stable low bacterial adhesion property. Since E. coli adheres on the control planar PS and TiO<sub>2</sub> surfaces over time, the results are related to the inherent bacteria releasing property of these nanopillars (especially the TiO<sub>2</sub> nanopillars) rather than their antifouling properties.

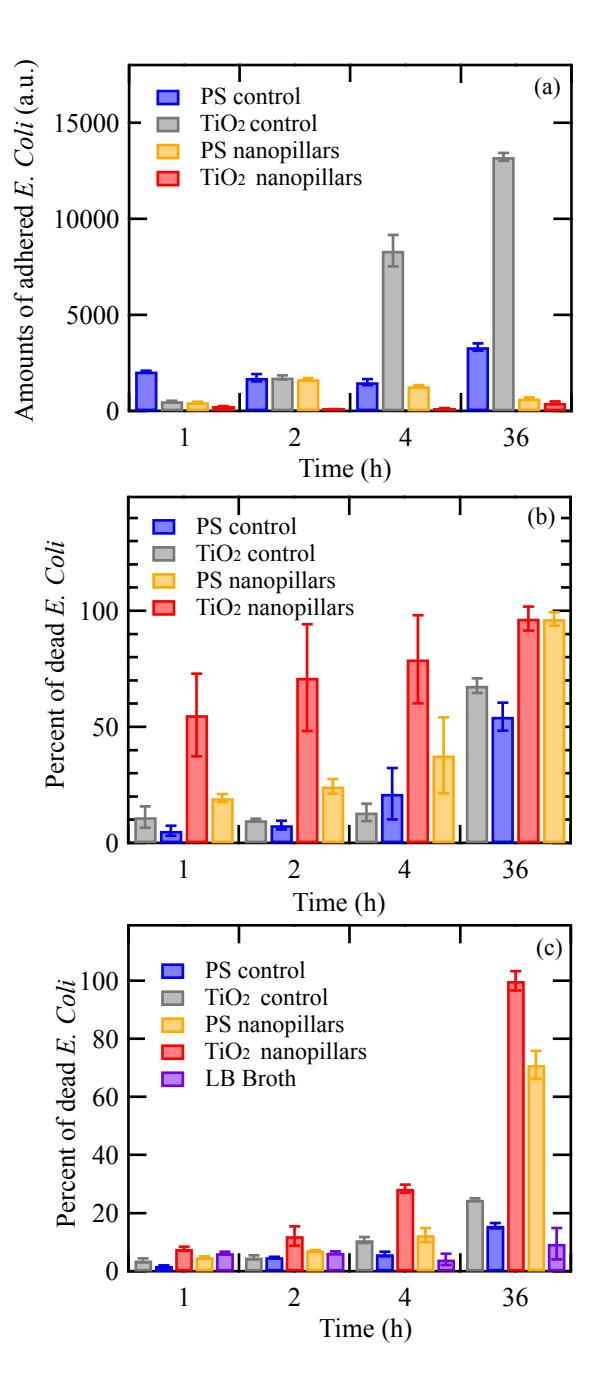


**Figure 4**. (a) Time dependence of the amount of adhered *E. coli* after incubating the samples, (b) the percentage of dead *E. coli* adhered onto the sample surfaces, (c) the percentage of dead *E. coli* extracted from the well solution (LB broth) for the planar PS thin film (15 nm thick), the planar TiO<sub>2</sub> thin film (3 nm thick), the PS nanopillars, and TiO<sub>2</sub> nanopillars.

**Figure 4b** shows the ratio of dead bacteria to the number of total bacteria adhered onto the nanopillar surfaces as a function of incubation time. The data clearly indicate that these nanopillars have improved bactericidal properties with good stability. Intriguingly, the bactericidal kinetics with the TiO<sub>2</sub> nanopillars were significantly improved: approximately half of adherent E. coli on the TiO<sub>2</sub> nanopillars were dead after only 1 hour of immersion. The kinetics are improved compared to nanostructured surfaces that closely mimic the dimensions of protrusions found in nature or nearly the same as that for sharper and taller nanopillars (i.e., h = 1.2-6.7  $\mu$ m and D = 280-600 nm)<sup>6</sup>. The percentage of dead cells adhered on the TiO<sub>2</sub> nanopillars reached nearly 100 % after 12 h of immersion, while more than 50 % of adherent E. coli on the flat TiO<sub>2</sub> surface were still alive under the same conditions. It should be noted that the PS nanopillars also showed more than 95% bacteria killing properties after 36 h of immersion, while the rate of bacteria death over time was much less effective compared to that of the TiO<sub>2</sub> nanopillars under the same conditions.

We also analyzed the percentage of dead *E. coli* in the LB broth taken after submersion of the nanopillars for up to 36 h. **Figure 4c** shows the fraction of dead *E. coli* relative to the total number of *E. coli* in the LB broth. At the respective time intervals, the LB broth was extracted from the wells, plated, and analyzed on glass coverslips. For a control, we also plot the percent of dead *E. coli* in the LB broth to account for the natural cell death after the same incubation period. We first demonstrated that the natural death rate in the LB medium is less than 10% even for the incubation time of 36 h, allowing for meaningful conclusions to be made about the effectiveness of the nanopillars. Next, we can also see that the rate of dead *E. coli* in the solutions with the nanopillars increases with the incubation time. Interestingly, the TiO<sub>2</sub> nanopillars are much more efficient, resulting in nearly 100 % death of *E. coli* in the LB broth after 36 h of immersion. For comparison, the percentages of the bacteria death in the control LB broth in the presence of the flat PS and TiO<sub>2</sub> sample were about 15% and 25 % after 36 h of immersion, respectively (**Figure 4c**). Therefore, the sets of data summarized in Figure 4 provide the evidence that *E. coli* is killed at the nanopillars surface and subsequently released in the solution instead of remaining as debris on the nanopillars.

Antimicrobial materials have a certain need for durability, and it is necessary to examine their efficacy over a prolonged period. To address this issue, we conducted additional bacterial adhesion experiments with the  $TiO_2$  nanopillars for up to 120 h by replenishing the bacterial broth with fresh LB medium and bacteria every 24 h. The results demonstrate that the total number of *E. coli* adhered to the  $TiO_2$  nanopillar surfaces was about 100 and the ratio of dead bacteria to the number of total bacteria adhered to the  $TiO_2$  nanopillar surfaces was  $94 \pm 6\%$ , which remained nearly unchanged compared to the data after 36 h of immersion (**Figure 4**). Hence, we draw the conclusion that the bactericidal and bacteria releasing properties of the  $TiO_2$  nanopillars are intact even after 120 h of immersion.

Now the question arises: what is the mechanism underlying the emerging functions for such short (height of about 10 nm) nanopillars against E. coli? As shown in Fig. 3d and 3e, the mechanism of bacteria death is not direct piercing. In fact, according to Xie and co-workers, the pillar height of greater than 1  $\mu$ m<sup>15</sup> is required for penetration of our nanopillars (with the size of about 50 nm) into a lipid bilayer by gravity. If a bacterial cell wall is not penetrated after distorting around the nanopillars and settling on the supporting substrate, it would adhere on to the substrate, as shown in **Figure 3e**. The stretching of bacteria cell walls<sup>3-5, 7-9</sup> is then crucial for rupture. Below, we employ MD simulations to mimic the experimental situations and provide further insight into the mechanism underlying the resultant bactericidal property of the short nanopillars.

#### 3.3. MD simulations

Here, we present simulation results of planar bilayers interacting with substrates having hexagonally arranged hydrophilic pillars representing domains. The sizes of the hexagonally arranged pillars are  $D_i = 20\sigma$ ,  $d = 6.6\sigma$ , and the height of the nanopillars was fixed to  $h = 16.3\sigma$ , which is nearly equivalent to the PS and TiO<sub>2</sub> nanopillars. The bilayer was introduced  $1\sigma$  above the top of the pillars and allowed to relax while the interaction between the substrate and the lipid was turned off. Then the interaction between the lipids and the substrates were activated and the integrity of the bilayer was inspected as a function varying lipid head-to-substrate interaction

energy,  $\varepsilon_{H-S}$ . That is, we checked whether the bilayer that is in contact with the substrate has ruptured. The parameters of the lipid bilayer were chosen such that the lipid has a bending rigidity of 52.3 kT. The bending rigidity chosen here is similar to that of phospholipids with 30% cholesterol to model  $E \ coli^{24}$ . The equilibrium area per lipid  $A_l$  is 1.06  $\sigma^{261}$  for a tensionless bilayer; however, thermal undulations create tears in the bilayer hence we decreased  $A_l$  to 1.0  $\sigma^2$ .

**Figure 5** shows the final snapshots of MD simulation results for the pillars at different headsubstrate interactions: top view (**Figures 5a-d**) and cross-section view (**Figures 5e-g**). From the figure we can see that rupture of the bilayer occurs (i.e., the substrate surface indicated in purple

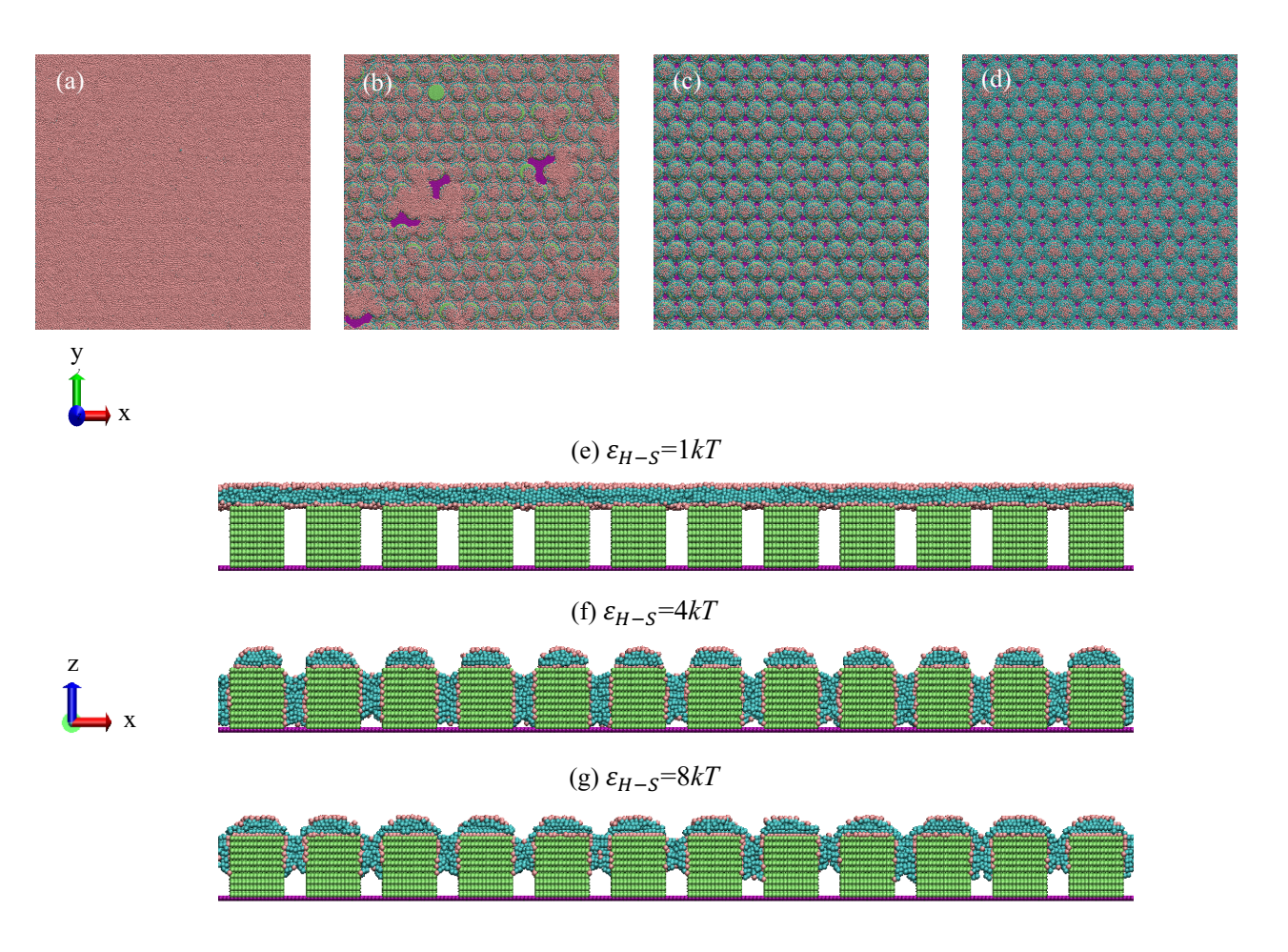


**Figure 5**. Final snapshots of simulations of a planar bilayer in contact with pillars at different head-substrate interaction strength: (a-d) top view and (e-g) cross-section view. (a), (b), (c) and (d) correspond to  $\varepsilon_{H-S}=1kT$ , 2kT, 4kT and 8kT, respectively. Lipid heads, lipid tails, and the pillars, and the substrate surface are indicated in metallic copper, turquoise, green, and purple, respectively.

is exposed) at the interaction strengths of  $\varepsilon_{H-S}=2kT$  and stronger (**Figures 5b-5d**). The bilayer at  $\varepsilon_{H-S}=1kT$  is stable on the pillars (i.e., the top surface is fully covered with lipid heads indicated by metallic copper), and no penetration of the pillars into the membrane takes place (Figures 5a and 5e). On the other hand, at  $\varepsilon_{H-S} \ge 2kT$ , the lipid heads strongly adsorb onto the pillar surfaces including the side walls of the pillars (Figures 5f and 5g), rearranging the bilayer to conform to the structure/curvature of the pillars. Further attractive interactions encourage additional membrane attachment, drawing the membrane taut against the pillars and inducing a membrane strain and tension. This tension would pull a bacteria cell wall (e.g., an outer lipid membrane for Gram-negative bacteria) taut against the pillar edge and generate a normal force that leads to rupturing the bilayer<sup>15</sup>. The breakage occurs at the high curvature regions near the edges of the pillars where the bilayer is subjected to high local stresses, as previously reported<sup>15</sup>. Furthermore, at  $\varepsilon_{H-S}=8kT$  (which is of the same magnitude of a E. coli/TiO<sub>2</sub> interaction), the lipid membrane does not reach the substrate surface when the lipid ruptures (Figure 5g). This indicates that much shorter pillars can kill E. coli if the head-substrate interaction is strongly attractive (e.g.,  $\varepsilon_{H-S}$ = 8kT). Additional MD simulations demonstrated that, at  $\varepsilon_{H-S}=8kT$ , the pillars with an  $8\sigma$ -height can penetrate the membrane, while the membrane is stable on the top of the pillars with a  $2\sigma$ height (Figure S10). Note that the thickness of the model bilayer is about  $5\sigma^{43}$ , and these results imply that rupture occurs if the features of a nanopatterned surface have length scales greater than the thickness of the bilayer. Hence, the MD results support the hypothesis that the PS and TiO<sub>2</sub> nanopillars (h = 10-14 nm) are sufficiently tall and attractive for rupturing lipid bilayers. Further computational studies along with experiments to identify the height-induced bactericidal transition deserve future work. The resultant physical damage to the bacterial outer cell membrane may cause increased uptake of a fluorescent dye (i.e., propidium Iodide) that do not normally enter the membranes of healthy cells $^{62}$ , indicating the death of a bacterium.

## 3.4. Releasing the bacterial cell debris

Both natural and synthetic superhydrophobic surfaces (i.e.,  $\theta_c > 150^\circ$ )<sup>63</sup> are believed to achieve a self-cleaning property by the so-called "lotus effect" associated with entrapping air bubbles between surface features<sup>64</sup>. However, as shown in **Figure 2**, water penetrates the cavities between the TiO<sub>2</sub> and PS nanopillars completely after a couple of hours such that the emergent self-cleaning properties of the PS and TiO<sub>2</sub> nanopillars cannot be explained by the lotus effect. Based on the present findings, we propose the following mechanism underlying the emergent bacteria releasing property of our nanopillar arrays. As indicated above, the attraction between the bacterial cell wall and nanopillars facilitates the adhesion of a bacteria cell wall and causes high local stresses in the wall near the edges of the nanopillars, leading to the outer cell wall rupture and the formation of pores between nanopillars. As the time goes by, more holes, ultimately, promote cell withdrawal from the nanopillar surface. As shown in Figure 4c, the number of dead E. coli after contact with the nanopatterned surface increases with increasing incubation time for at least 36 h. There may be remaining adhered portions (i.e., debris) of an outer membrane on the PS or TiO<sub>2</sub> nanopillars after the bacteria detachment. However, they are unstable since the hydrophobic region of the membrane is exposed to water, leading to the formation of micelle structures and detachment of the debris from the nanopillar surfaces.

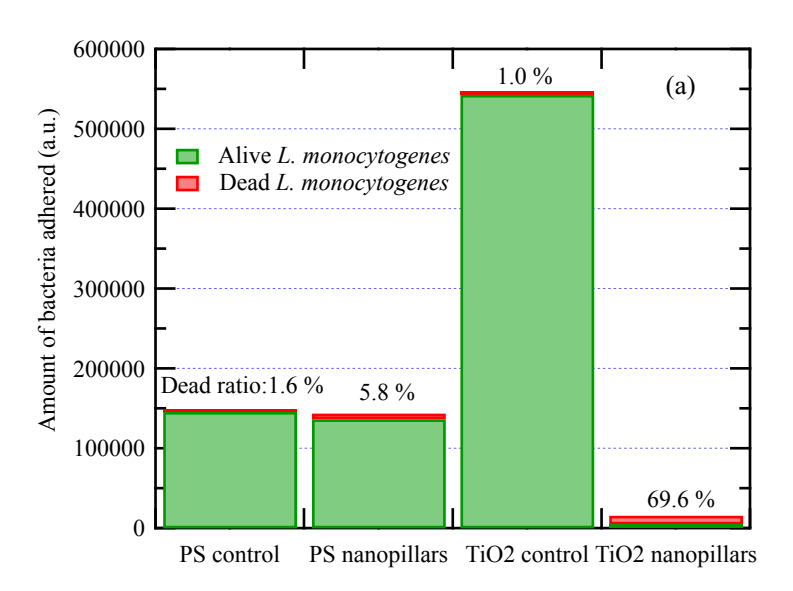
# 3.5. Gram-positive bacterium

We also conducted similar bacteria adhesion studies with *L. monocytogenes*, a Gram-positive bacterium surface energy of  $\gamma_b = 65.9 \text{ mJ/m}^2$  such that the bacteria-substrate interactions with PS or TiO<sub>2</sub> are very close to those of *E. coli*. In general, the mechano-bactericidal action with engineered random or ordered nanostructures is not effective against Gram-positive bacteria due to the much stiffer mechanical properties<sup>5, 10</sup>. The mechanical property difference is attributed to the thickness of a peptidoglycan layer<sup>41</sup> between Gram-negative (2.5-6.5 nm in thickness when fully hydrated) and Gram-positive (19-33 nm in thickness when fully hydrated) bacteria<sup>65</sup>. The peptidoglycan layer, which is composed of linear glycan strands that are cross-linked with short peptide, is also an important component of a bacteria cell wall which provides support against the

bacteria cell's internal osmotic pressure<sup>65</sup>. The experimental procedure consisted of the same protocol used for E. coli. Figure 6a summarizes the number of L. monocytogenes adhered on the control PS and TiO<sub>2</sub> substrates and the PS and TiO<sub>2</sub> nanopillars as well as the fraction of dead L. monocytogenes on them after 4 h of incubation. When compared to the results for E. coli shown in Figure 4, the efficiencies of the bactericidal and bacteria releasing properties against L. monocytogenes are very similar to those against E. coli. The result illustrates the versatile

antibacterial properties of the TiO<sub>2</sub> nanopillars against different types of bacteria. It should be noted that the bactericidal and bacteria releasing properties of the PS nanopillars against *L. monocytogenes* not significant (**Figure 6a**), suggesting that the peptidoglycan layer is likely not the only factor for directing the bactericidal property, as indicated previously<sup>6</sup>. The effect of the bacteria-substrate interaction should be underlined instead<sup>7</sup>.

As schematically shown in Figure 6b, when the bacteria membrane-substrate adhesion is strong, the bacteria cell wall continues to deform around the nanopillars until it eventually makes contacts with the surfaces. However, due to their inherent



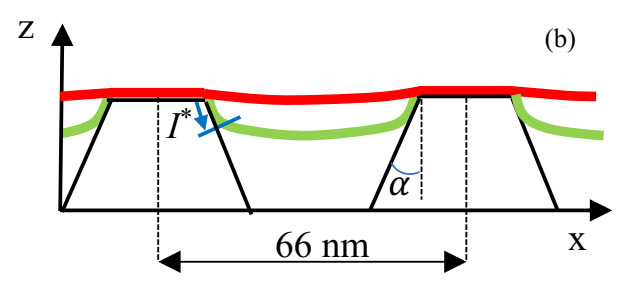


**Figure 6.** (a) Total amount of alive and dead L. *monocytogenes* adhered on the sample surfaces after 4h of incubation. The numbers on the bars correspond to the fraction of dead L. *monocytogenes* on the respective surfaces. (b) Illustration of the indentation distance  $(I^*)$ . The initial membrane shape is indicated as red. The green curve indicates the membrane shape at penetration. The blue arrow indicates the displacement of the membrane at penetration. As indicated in Figure 1c, the  $TiO_2$  nanopillars are cone shaped with a side wall angle  $(\alpha)$  of about 15°.

stiffness, Gram-positive bacterial cells adapt a flatter membrane profile, limiting the adhesion area to the nanopillar surface and hence creating higher stress concentrations within a bacteria cell wall (i.e., the driving force for rupture) at the edge of nanopillars compared to Gram-negative bacterium cells<sup>15</sup>. Xie and co-workers calculated that for nanopillars with d = 100 nm, which is double the size of the TiO<sub>2</sub> nanopillars, a stiff membrane (whose Young's modulus is 9 times higher than that of a pure lipid bilayer) requires only a 5 nm "indentation distance" ( $I^*$ , see **Figure 6b**) along the nanopillar surface for rupture<sup>15</sup>. In other words, only a small deformation of a cell wall prompted by a bacteria-substrate interaction would be sufficient for cell wall rupture. From **Figure 6a**, the interaction of L monocytogenes with TiO<sub>2</sub> is better than that of PS (i.e., more L monocytogenes adhered on the planar TiO<sub>2</sub> surface than the planar PS surface). Hence, as for E coli, we anticipate that the adhesion-mediated rupture plays a vital role for the initial step involved in the bactericidal action against L monocytogenes.

However, the detailed mechanisms underlying the emerging bactericidal and bacteria releasing properties of the TiO<sub>2</sub> nanopillars against *L. monocytogenes* need to be further clarified. The challenge is the lack of information on the exact nature of how the components of the peptidoglycan layer are organized in the bacterial cell wall, rendering molecular modeling and simulations difficult. Very recently, Chapagain and co-workers developed an atomistic model of the peptidoglycan layer of *Staphylococcus aureus* (*S. aureus*, a Gram-positive bacterium)<sup>66</sup>. Motivated by their results, bacteria adhesion experiments and simulations with *S. aureus* are in progress to address (i) how repeating disaccharide (sugar) units (i.e., the skeleton of a peptidoglycan mesh) in the peptidoglycan layer is broken off during the bactericidal action and (ii) how debris of a peptidoglycan layer on the nanopillar surfaces after the bacteria detachment (if any) becomes unstable.

## 4. Conclusions

In summary, we have revealed multifunctional antibacterial properties of the vertically aligned nanostructures created via self-assembly of PS-*block*-PMMA block copolymers. The cross-linked

PS cylinders without a PMMA matrix ("PS nanopillars") were used as a rational system. The PS nanopillars exhibit not only highly effective mechano-bactericidal actions but also highly effective bacteria releasing properties against *E. coli* during at least 36 h of immersion in a *E. coli* solution. To understand the mechanism, we deposited a thin ALD-grown TiO<sub>2</sub> film (about 3 nm thick) on top of the PS nanopillar surfaces ("TiO<sub>2</sub> nanopillars"), which allowed us to use the bacteria-solid interaction as a thermodynamic criterion for predicting bacterial adhesion. Interestingly, the efficacy of the TiO<sub>2</sub> nanopillars was further improved along with the enhanced bactericidal kinetics, compared to the PS nanopillars. We also found that the TiO<sub>2</sub> nanopillars exhibited the bactericidal and bacteria releasing properties against *L. monocytogenes*, a Gram-positive bacterium, while the properties of the PS nanopillars against *L. monocytogenes* were not significant.

To provide the insight into the mechanism underlying the multifaceted functionality of such short nanopillars and the effect of the TiO<sub>2</sub> layer on the improved functionalities, implicit solvent coarse-grained MD simulations of a lipid bilayer, which is in contact with a substrate containing cylindrical hydrophilic pillars with different lipid-substrate interactions, were performed as a simplified model for E. coli. The MD results demonstrated that when the bacterium/substrate interaction is attractive, the lipid heads strongly adsorb onto the hydrophilic pillar surfaces, conforming the shape of the lipid bilayer to the structure/curvature of the pillars. A better attractive interaction further encourages additional membrane attachment to the pillar surfaces. Membrane rupture occurs when the pillars generate sufficient tension within the lipid bilayer clamped at the edges of pillars. This situation would be easier for Gram-positive bacteria since the adhesion area to the pillar surface is limited, creating higher stress concentrations within the bacterial cell wall. A small additional deformation of the bacterial cell associated with attractive nanopatterned surfaces is then sufficient for rupture. Further MD simulations for hydrophobic nanopatterned surfaces with different domain geometries, shapes, and bacterium/substrate interactions are in progress for a better understanding of nano-bio interactions to enable rationally guided design strategies for advanced multifunctional surface coatings for implantable medical devices.

Utilizing block copolymer materials allows us to fabricate highly ordered patterns at length

scales not achievable for common imprinting and lithography techniques. These materials can be

manipulated to yield various pattern arrays even on flexible and non-flat surfaces (e.g., catheters)

using dip-coating. Nonetheless, more research needs to be done to investigate the durability of the

nanopillars with the wear and tear experienced by, for example, a catheter in medical use. The

concept and strategy for creating multifunctional coatings are translatable to other implantable

medical devices composed of metals such as stents. Moreover, nanostructured surfaces play vital

roles in controlling cell adhesion and function<sup>67-68</sup> and platelet adhesion and activation for

clotting<sup>69</sup>. Motivated by these results, interactions of the nanopillars with cell and platelet are

currently in progress.

**Author Information** 

**Corresponding Authors** 

Email: tadanori.koga@stonybrook.edu (T. K.)

Email: maya.koga@stonybrook.edu (M. E.)

**Author Contributions** 

The manuscript was written through contributions of all authors. All authors have given approval

to the final version of the manuscript.

**Notes** 

The authors declare no competing financial interest.

Acknowledgements

T.K. acknowledges partial financial support from National Science Foundation (NSF DGE

1922639 and DMR Polymers 2210207). M.E. and T.K. also acknowledge partial financial support

from the International Collaborative Research Program of Institute for Chemical Research, Kyoto

30

University (grant # 2022-96). We thank Sayantani Sikder and Xiao Tong for helping us conduct the XPS experiments. The computational/simulations aspect of this work were performed at the Center for Nanophase Materials Sciences, a U.S. Department of Energy Office of Science User Facility, operated at Oak Ridge National Laboratory. This research also used resources of the Oak Ridge Leadership Computing Facility, which is a DOE Office of Science User Facility supported under Contract DE-AC05-00OR22725. This work used resources of the Center for Functional Nanomaterials and the National Synchrotron Light Source II (Beamline 11-BM), which are U.S. DOE Office of Science User Facilities, at Brookhaven National Laboratory under Contract No. DE-SC0012704.

## **Supporting Information Available.**

- Figure S1. XPS spectrum of the TiO<sub>2</sub> nanopillars.
- Figure S2. Water contact angle of a PS thin film before and after UV exposure.
- Figure S3. Simulation snapshots of a planar bilayer in contact with nanopillars.
- Figure S4. Evolution of the total system energy for the system with  $\varepsilon_{H-S} = 4kT$ .
- Figure S5. Detailed characterization of the PS nanopillars using AFM and GISAXS.
- Figure S6. Representative 2D GISAXS profile for the TiO<sub>2</sub> nanopillars.
- Figure S7. Time dependence of water contact angle for the PS and TiO<sub>2</sub> nanopillars.
- Figure S8. XPS data of the PS nanopillars and the detailed analysis.
- Figure S9. Scattering intensity from a water droplet on the TiO<sub>2</sub> nanopillars.
- Figure S10. Simulation snapshots of a planar bilayer in contact with shorter nanopillars.
- Table S1. Force-field parameters used for the MD simulations.
- Discussion about water contact angle based on the theoretical models.

This material is available free of charge *via* the Internet at http://pubs.acs.org.

## References

- (1) Greene, L.; Marx, J.; Oriola, S., Guide to the Elimination of Catheter-Associated Urinary Tract Infections (CAUTIs). The Association for Professionals in Infection Control and Epidemiology (APIC) Washington, DC, 2008.
- (2) Jacobsen, S. M.; Stickler, D. J.; Mobley, H. L.; Shirtliff, M. E. Complicated Catheter-associated Urinary Tract Infections due to Escherichia coli and Proteus Mirabilis. *Clin. Microbiol. Rev.* **2008**, *21*, 26-59.
- (3) Linklater, D. P.; Baulin, V. A.; Juodkazis, S.; Crawford, R. J.; Stoodley, P.; Ivanova, E. P. Mechano-bactericidal Actions of Nanostructured Surfaces. *Nat. Rev. Microbiol.* **2021**, *19*, 8-22.
- (4) Ivanova, E. P.; Hasan, J.; Webb, H. K.; Truong, V. K.; Watson, G. S.; Watson, J. A.; Baulin, V. A.; S.Pogodin; Wang, J. Y.; Tobin, M. J.; Löbbe, C.; Crawford, R. J. Natural Bactericidal Surfaces: Mechanical Rupture of Pseudomonas aeruginosa Cells by Cicada Wings. *Small* **2012**, *8*, 2489-2494.
- (5) Pogodin, S.; Hasan, S.; Baulin, V. A.; Webb, H. K.; Truong, V. K.; Nguyen, H. N.; Boshkovikj, V.; Fluke, C. J.; Watson, G. S.; Watson, J. A.; Crawford, R. J.; Ivanova, E. P. Biophysical Model of Bacterial Cell Interactions with Nanopatterned Cicada Wing Surfaces. *Biophys. J.* **2013**, *104*, 835-840.
- (6) Michalska, M.; Gambacorta, F.; Divan, R.; Aranson, I. S.; Sokolov, A.; Noirot, P.; Laible, P.
  D. Tuning Antimicrobial Properties of Biomimetic Nanopatterned Surfaces. *Nanoscale* 2018, 10, 6639-6650.
- (7) Hasan, J.; Jain, S.; Chatterjee, K. Nanoscale Topography on Black Titanium Imparts Multibiofunctional Properties for Orthopedic Applications. *Sci. Rep.* **2017**, *7*, 41118.
- (8) Wu, S.; Zuber, F.; Maniura-Weber, K.; Brugger, J.; Ren, Q. Nanostructured Surface Topographies Have an Effect on Bactericidal Activity. *J. Nanobiotechnol.* **2018**, *16*, 1-9.
- (9) Vassallo, E.; Pedroni, M.; Silvetti, T.; Morandi, S.; Toffolatti, S.; Angella, G.; Brasca, M. Bactericidal Performance of Nanostructured Surfaces by Fluorocarbon Plasma. *Mater. Sci. Eng. C.* **2017**, *80*, 117–121.

- (10) Bhadra, C. M.; Werner, M.; Baulin, V. A.; Truong, V. K.; Kobaisi, M. A.; Nguyen, S. H.; Balcytis, A.; Juodkazis, S.; Wang, J. Y.; Mainwaring, D. E.; Crawford, R. J.; Ivanova, E. P. Subtle Variations in Surface Properties of Black Silicon Surfaces Influence the Degree of Bactericidal Efficiency. *Nano-Micro Lett.* **2018**, *10*, 36-1-8.
- (11) Xue, F.; Liu, J.; Guo, L.; Zhang, L.; Li, Q. Theoretical Study on the Bactericidal Nature of Nanopatterned Surfaces. *J. Theor. Biol.* **2015**, *385*, 1-7.
- (12) Li, X. Bactericidal Mechanism of Nanopatterned Surfaces. *Phys. Chem. Chem. Phys.* **2016**, *18*, 1311-1316.
- (13) Ivanova, E. P.; Linklater, D. P.; Werner, M.; Baulin, V. A.; Xu, X.; Vrancken, N.; Rubanov, S.; Hanssen, E.; Wandiyanto, J.; Truong, V. K.; Elbourne, A.; Maclaughlin, S.; Juodkazis, S.; Crawford, R. J. The Multi-faceted Mechano-bactericidal Mechanism of Nanostructured Surfaces. *Proc. Natl. Acad. Sci. U.S.A.* **2020**, *117*, 12598–12605.
- (14) Jenkins, J.; Mantell, J.; Neal, C.; Gholinia, A.; Verkade, P.; Nobbs, A. H.; Su, B. Antibacterial Effects of Nanopillar Surfaces are Mediated by Cell Impedance, Penetration and Induction of Oxidative Stress. *Nat. Commun.* **2020**, *11*, 1626.
- (15) Xie, X.; Xu, A. M.; Angle, M. R.; Tayebi, N.; Verma, P.; Melosh, N. A. Mechanical Model of Vertical Nanowire Cell Penetration. *Nano Lett.* **2013**, *13*, 6002-6008.
- (16) Linklater, D. P.; Juodkazis, S.; Rubanov, S.; Ivanova, E. P. Comment on "Bactericidal Effects of Natural Nanotopography of Dragonfly Wing on Escherichia Coli". *ACS Appl. Mater. Interfaces* **2017**, *9*, 29387-29393.
- (17) Valiei, A.; Lin, N.; McKay, G.; Nguyen, D.; Moraes, C.; Hill, R. J.; Tufenkji, N. Surface Wettability Is a Key Feature in the Mechano-Bactericidal Activity of Nanopillars. *ACS Appl. Mater. Interfaces* **2022**, *14*, 27564-27574.
- (18) Boinovich, L. B.; Modin, E. B.; Aleshkin, A. V.; Emelyanenko, K. A.; Zulkarneev, E. R.; Kiseleva, I. A.; Vasiliev, A. L.; Emelyanenko, A. M. Effective Antibacterial Nanotextured Surfaces Based on Extreme Wettability and Bacteriophage Seeding. *ACS Appl. Nano Mater.* **2018**, *1*, 1348–1359.

- (19) Jiang, R.; Yi, Y.; Hao, L.; Chen, Y.; Tian, L.; Dou, H.; Zhao, J.; Ming, W.; Ren, L. Thermoresponsive Nanostructures: From Mechano-Bactericidal Action to Bacteria Release. *ACS Appl. Mater. Interfaces* **2021**, *13*, 60865–60877.
- (20) Hawker, C. J.; Russell, T. P. Block Copolymer Lithography: Merging "Bottom-Up" with "Top-Down" Processes. *MRS Bulletin* **2005**, *30*, 952-966.
- (21) Segalman, R. A. Patterning with block copolymer thin films. *Mater. Sci. Eng., R* **2005,** 48, 191–226.
- (22) Morimitsu, Y.; Salatto, D.; Jiang, N.; Sen, M.; Nishitsuji, S.; Yavitt, B. M.; Endoh, M. K.; Subramanian, A.; Nam, C.-Y.; Li, R.; Fukuto, M.; Zhang, Y.; Wiegart, L.; Fluerasu, A.; Tanaka, K.; Koga, T. "Structurally Neutral" Densely Packed Homopolymer-Adsorbed Chains for Directed Self-Assembly of Block Copolymer Thin Films. *Macromolecules* **2019**, *52*, 5157-5167.
- (23) Kamcev, J.; Germack, D. S.; Nykypanchuk, D.; Grubbs, R. B.; Nam, C.-Y.; Black, C. T. Chemically Enhancing Block Copolymers for Block-Selective Synthesis of Self-Assembled Metal Oxide Nanostructures. *ACS Nano* **2013**, *7*, 339-346.
- (24) Sibilo, R.; Mannelli, I.; Reigada, R.; Manzo, C.; Noyan, M. A.; Mazumder, P.; Pruneri, V. Direct and Fast Assessment of Antimicrobial Surface Activity Using Molecular Dynamics Simulation and Time-Lapse Imaging. *Anal. Chem.* **2020**, *92*, 6795-6800.
- (25) Stevens, M. M.; George, J. H. Exploring and Engineering the Cell Surface Interface. *Science* **2005**, *310*, 1135-1138.
- (26) Jiang, N.; Shang, J.; Di, X.; Endoh, M. K.; Koga, T. Formation Mechanism of High-Density, Flattened Polymer Nanolayers Adsorbed on Planar Solids. *Macromolecules* **2014**, *47*, 2682-2689.
- (27) Gin, P.; Jiang, N.; Liang, C.; Taniguchi, T.; Akgun, B.; Satija, S. K.; Endoh, M. K.; Koga, T. Revealed Architectures of Adsorbed Polymer Chains at Solid-Polymer Melt Interfaces. *Phys. Rev. Lett.* **2012**, *109*, 265501.
- (28) Kim, T.; Wooh, S.; Son, J. G.; Char, K. Orientation Control of Block Copolymer Thin Films Placed on Ordered Nanoparticle Monolayers. *Macromolecules* **2013**, *46*, 8144-8151.

- (29) Sultanova, N.; Kasarova, S.; Nikolov, I. Dispersion Properties of Optical Polymers. *Acta Physica Polonica*, A. **2009**, *116*, 585-587.
- (30) Liu, L.; Bhatia, R.; Webster, T. J. Atomic layer deposition of nano-TiO<sub>2</sub> thin films with enhanced biocompatibility and antimicrobial activity for orthopedic implants. *Int. J. Nanomed.* **2017**, *12*, 8711-8723.
- (31) Giavaresi, G.; Ambrosio, L.; Battiston, G. A.; Casellato, U.; Gerbasi, R.; Finia, M.; Aldini, N. N.; Martini, L.; Rimondini, L.; Giardino, R. Histomorphometric, Ultrastructural and Microhardness Evaluation of the Osseointegration of a Nanostructured Titanium Oxide Coating by Metal-organic Chemical Vapour Deposition: an In Vivo Study. *Biomaterials* **2004**, *25*, 5583-5591.
- (32) Chaukulkar, R.; Agarwal, S. Atomic Layer Deposition of Titanium Dioxide Using Titanium Tetrachloride and Titanium Tetraisopropoxide as Precursors. *J. Vac. Sci. Technol. A.* **2013**, *31*, 031509.
- (33) X. Zhang; Q. Zhang; T. Yan; Z. Jiang; X. Zhang; Y. Y. Zuo. Quantitatively Predicting Bacterial Adhesion Using Surface Free Energy Determined with a Spectrophotometric Method. *Environ. Sci. Technol.* **2015**, *49*, 6164–6171.
- (34) Mafu, A. A.; Roy, D.; Goulet, J.; Savoie, L. Characterization of Physicochemical Forces Involved in Adhesion of Listeria Monocytogenes to Surfaces. *Appl. Environ. Microbiol.* **1991,** *57*, 1969-1973.
- (35) Wang, L.; Zhou, Y.; Yang, Y.; Subramanian, A.; Kisslinger, K.; Zuo, X.; Chuang, Y.-C.; Yin, Y.; Nam, C.-Y.; Rafailovich, M. H. Suppression of Carbon Monoxide Poisoning in Proton Exchange Membrane Fuel Cells via Gold Nanoparticle/Titania Ultrathin Film Heterogeneous Catalysts. *ACS Appl. Energy Mater.* **2019**, *2*, 3479-3487.
- (36) Piercy, B. D.; Leng, C. Z.; Losego, M. D. Variation in the Density, Optical Polarizabilities, and Crystallinity of TiO<sub>2</sub> Thin Films Deposited via Atomic Layer Deposition from 38 to 150 °C Using the Titanium Tetrachloride-water Reaction. *J. Vac. Sci. Technol. A* **2017**, *35*, 03E107.

- (37) Liu, K.; Jiang, L. Bio-Inspired Self-Cleaning Surfaces. *Annu. Rev. Mater. Res.* **2012**, *42*, 231–263.
- (38) Ilavsky, J.; Jemian, P. R. Irena Tool Suite for Modeling and Analysis of Small-angle Scattering. *J. Appl. Cryst.* **2009**, *42*, 347-353.
- (39) Hou, S.; Gu, H.; Smith, C.; Ren, D. Microtopographic Patterns Affect Escherichia coli Biofilm Formation on Poly(dimethylsiloxane) Surfaces. *Langmuir* **2011**, *27*, 2686-2691.
- (40) Jamshidi, A.; Zeinali, T. Significance and Characteristics of Listeria Monocytogenes in Poultry Products. *Int. J. Food Sci.* **2019**, *2019*, 7835253.
- (41) Purushothaman, S.; Cicuta, P.; Ces, O.; Brooks, N. J. Influence of High Pressure on the Bending Rigidity of Model Membranes. *J. Phys. Chem. B* **2015**, *119*, 9805–9810.
- (42) Brown, W. M.; Wang, P.; Plimpton, S. J.; Tharrington, A. N. Implementing Molecular Dynamics on Hybrid High Performance Computers—short Range Forces. *Comput. Phys. Commun.* **2011**, *182*, 898-911.
- (43) Carrillo, J.-M. Y.; Katsaras, J.; Sumpter, B. G.; Ashkar, R. A Computational Approach for Modeling Neutron Scattering Data from Lipid Bilayers. *J. Chem. Theory Comput.* **2017**, *13*, 916-925.
- (44) Cooke, I. R.; Deserno, M. Solvent-free Model for Self-assembling Fluid Bilayer Membranes: Stabilization of the Fluid Phase Based on Broad Attractive Tail Potentials. *J. Chem. Phys.* **2005**, *123*, 224710
- (45) Kremer, K.; Grest, G. S. Dynamics of Entangled Linear Polymer Melts a Molecular-Dynamics Simulation. *J. Chem. Phys.* **1990**, *92*, 5057-5086.
- (46) Salatto, D.; Carrillo, J.-M. Y.; Endoh, M. K.; Taniguchi, T.; Yavitt, B. M.; Masui, T.; Kishimoto, H.; Tyagi, M.; Ribbe, A. E.; Sakai, V. G.; Kruteva, M.; Sumpter, B. G.; Farago, B.; Richter, D.; Nagao, M.; Koga, T. Structural and Dynamical Roles of Bound Polymer Chains in Rubber Reinforcement. *Macromolecules* **2021**, 54, 11032-11046.
- (47) Absolom, D. R.; Lamberti, F. V.; Policova, Z.; Zingg, W.; van Oss, C. J.; Neumann, A. Surface Thermodynamics of Bacterial Adhesion. *Appl. Environ. Microbiol.* **1983**, *46*, 90–97.

- (48) Sharma, P. K.; Rao, K. H. Analysis of Different Approaches for Evaluation of Surface Energy of Microbial Cells by Contact Angle Goniometry. *Adv. Colloid Interface Sci.* **2002**, *98*, 341–463.
- (49) Kwok, D. Y.; Neumann, A. W. Contact Angle Measurement and Contact Angle Interpretation. *Adv. Colloid Interface Sci.* **1999**, *81*, 167–249.
- (50) Jiang, N.; Sen, M.; Zeng, W.; Chen, Z.; Cheung, J.; Morimitsu, Y.; Endoh, M. K.; Koga, T.; Fukuto, M.; Yuan, G.; Satija, S. K.; Carrillo, J.-M. Y.; Sumpter, B. G. Structure-induced Switching of Interpolymer Adhesion at a Solid–polymer Melt Interface. *Soft Matter* **2018**, *14*, 1108-1119.
- (51) Wu, S. Calculation of Interfacial Tension in Polymer Systems. *J. Polym. Sci., Part C: Polym. Symp.* **1971,** *34*, 19-30.
- (52) Delalande, M.; Cunge, G.; Chevolleau, T.; Bezard, P.; Archambault, S.; Joubert, O. Development of Plasma Etching Processes to Pattern Sub-15 nm Features with PS-b-PMMA Block Copolymer Masks: Application to Advanced CMOS Technology. *J. Vac. Sci. Technol. B* **2014**, *32*, 051806.
- (53) Quéré, D. Rough Ideas on Wetting. Phys. A 2002, 313, 32-46.
- (54) Wenzel, R. N. Resistance of Solid Surfaces to Wetting by Water. *Ind. Eng. Chem.* **1936,** 28, 988–994.
- (55) Xu, X.; Vereecke, G.; Chen, C.; Pourtois, G.; Armini, S.; Verellen, N.; Tsai, W.-K.; Kim, D.-W.; Lee, E.; Lin, C.-Y.; Dorpe, P. V.; Struy, H.; Holsteyns, F.; V.Moshchalkov; Indekeu, J.; Gendt, S. D. Capturing Wetting States in Nanopatterned Silicon. *ACS Nano* **2014**, *8*, 885-893.
- (56) Checco, A.; Hofmann, T.; DiMasi, E.; Black, C. T.; Ocko, B. M. Morphology of Air Nanobubbles Trapped at Hydrophobic Nanopatterned Surfaces. *Nano Lett.* **2010**, *10*, 1354-1358.
- (57) Hura, G.; Russo, D.; Glaeser, R. M.; Head-Gordon, T.; Krack, M.; Parrinello, M. Water Structure as a Function of Temperature from X-ray Scattering Experiments and Ab Initio Molecular Dynamics. *Phys. Chem. Chem. Phys.* **2003**, *5*, 1981-1991.
- (58) Hwang, G. B.; Page, K.; Patir, A.; Nair, S. P.; Allan, E.; Parkin, I. P. The Anti-Biofouling Properties of Superhydrophobic Surfaces are Short-Lived. *ACS Nano* **2018**, *12*, 6050–6058.

- (59) Ivanova, E. P.; Hasan, J.; Webb, H. K.; Gervinskas, G.; Juodkazis, S.; Truong, V. K.; Wu, A. H. F.; Lamb, R. N.; Baulin, V. A.; Watson, G. S.; Watson, J. A.; Mainwaring, D. E.; Crawford, R. J. Bactericidal Activity of Black Silicon. *Nat. Commun.* **2013**, *4*, 2838.
- (60) Finkel, S. E. Long-term Survival During Stationary Phase: Evolution and the GASP Phenotype. *Nat. Rev. Microbiol.* **2006**, *4*, 113-120.
- (61) Carrillo, J.-M. Y.; Katsaras, J.; Sumpter, B. G.; Ashkar, R. A Computational Approach for Modeling Neutron Scattering Data from Lipid Bilayers. *J. Chem. Theory Comput.* **2017**, *13*, 916–925.
- (62) Benito, A.; Ventoura, G.; Casadei, M. A.; Robinson, T. P.; Mackey, B. M. Variation in Resistance of Natural Isolates of Escherichia coli O157 to High Hydrostatic Pressure, Mild Heat, and Other Stresses. *Appl. Environ. Microbiol.* **1999**, *65*, 1565-1569.
- (63) Quéré, D. Wetting and Roughness. Annu. Rev. Mater. Res. 2008, 38, 71099.
- (64) Blossey, R. Self-cleaning Surfaces-virtual Realities. Nat. Mater. 2003, 2, 301–306.
- (65) Auer, G. K.; Weibel, D. B. Bacterial Cell Mechanics. Biochenistry 2017, 56, 3710-3724.
- (66) Pokhrel, R.; Shakya, R.; Baral, P.; Chapagain, P. Molecular Modeling and Simulation of the Peptidoglycan Layer of Gram-Positive Bacteria Staphylococcus Aureus. *J. Chem. Inf. Model.* **2022**, *62*, 4955–4962.
- (67) Bettinger, C. J.; Langer, R.; Borenstein, J. T. Engineering Substrate Topography at the Microand Nanoscale to Control Cell Function. *Angew. Chem. Int. Ed.* **2009**, *48*, 5406-5415.
- (68) Jeon, H.; Koo, S.; Reese, W. M.; Loskill, P.; Grigoropoulos, C. P.; Healy, K. E. Directing Cell Migration and Organization via Nanocrater-patterned Cell-repellent Interfaces. *Nat. Mater.* **2015**, *14*, 918-923.
- (69) Koh, L. B.; Rodriguez, I.; Venkatraman, S. S. The Effect of Topography of Polymer Surfaces on Platelet Adhesion. *Biomaterials* **2010**, *31*, 1533-1545.